Research article **Open Access**

Hyunyoung Y. Kim and Daisik S. Kim*

Selection rule engineering of forbidden transitions of a hydrogen atom near a nanogap

DOI 10.1515/nanoph-2017-0037
Received March 29, 2017; revised April 25, 2017; accepted May 2, 2017

Abstract: We perform an analytical study on the allowance of forbidden transitions for a hydrogen atom placed near line dipole sources, mimicking light emanating from a one-dimensional metallic nanogap. It is shown that the rapid variation of the electric field vector, inevitable in the near zone, completely breaks the selection rule of $\Delta l = \pm 1$. While the forbidden transitions between spherically symmetric S states, such as 2S to 1S or 3S to 1S ($\Delta l = 0$), are rather robust against selection rule breakage, $\Delta l = \pm 2$ transitions such as between 3D and 1S or 3D and 2S states are very vulnerable to the spatial variation of the perturbing electric field. Transitions between 2S and 3D states are enhanced by many orders of magnitude, aided by the quadratic nature of both the perturbing Hamiltonian and D wavefunctions. The forbidden dipole moment, which approaches one Bohr radius times the electric charge in the vicinity of the gap, can be written in a simple closed form owing to the one-dimensional nature of our gap. With large enough effective volume together with the symmetric nature of the excited state wavefunctions, our work paves way towards atomic physics application of infinitely long nanogaps.

Keywords: nanogap; selection rule; forbidden transition; quantum plasmonics.

1 Introduction

Long wavelength approximation is at the heart of well-known selection rules in atomic spectroscopy. The wavelength of light is much larger than the atom size, so that the light-atom interaction Hamiltonian can safely ignore the spatial variation in the scale of the wavelength, resulting in an effective Hamiltonian in the form of $-\vec{p}\cdot\vec{E} = -e\vec{x}\cdot\hat{\varepsilon}E_0 e^{-i\omega t}$ where $\vec{p}$ is the dipole moment operator, $\vec{E}$ the electric field of light, $\hat{\varepsilon}$ the polarization direction unit vector, E_0 the amplitude of the electric field, and ω the angular frequency of light. Thereby, spontaneous emission, stimulated emission, and absorption are all proportional to the matrix element $\langle \psi_f | \vec{x} | \psi_i \rangle$ (ψ_f, ψ_i = final and initial state wavefunctions, respectively), from which all selection rules follow. The most important selection rule $\Delta l = \pm 1$; $\Delta m = \pm 1$, 0 originates from the position operator $\vec{x}$ being represented by the spherical harmonics of order 1. While this selection rule can be broken by magnetic dipole transition, electric quadrupole transition, or by two photon transitions, these forbidden transitions are typically several orders of magnitudes weaker. For instance, the 2P-1S allowed transition lifetime of 2 ns for a hydrogen atom compares favorably with 4.6 days for the forbidden magnetic dipole transition lifetime of 2S to 1S. On the other hand, the electric quadrupole transition between 3D and 2S is somewhat less forbidden, taking 20 ms [1, 2]. Of some practical importance, this one-photon lifetime of the forbidden magnetic dipole transition between 2S and 1S is so impractically long that it is easily superseded by the two-photon lifetime of 0.15 s [3], which played an important role in the measurements of the Lamb shift [4].

While the spatial variation of electromagnetic waves in free space occurs within the wavelength scale, close to the induced sources such as surface current and surface charges which naturally occur in metallic nano objects, electric field vectors can vary in length scale much smaller than their vacuum wavelength, in the length scale of the nano objects themselves or the gap size between the metallic objects [5–19]. Of particular interest in the present paper is the one-dimensional metallic nano- and sub-nanogaps whose widths can be in the 1–0.1 nm regime [17–19], comparable to the spatial extents of hydrogen atom wavefunctions while maintaining a macroscopic length of 1 mm to 1 cm. Electric fields emanating from these gaps possess rapidly varying electric fields, both in magnitude and in direction, in the length scale of the gap itself, creating a potentially very useful field configuration for the

***Corresponding author: Daisik S. Kim,** Department of Physics and Astronomy, Seoul National University, Seoul 151-747, Korea, e-mail: dsk@phya.snu.ac.kr.
Hyunyoung Y. Kim: Department of Physics, Korea University, Seoul 02841, Korea

purpose of breaking down well-known selection rules, thereby facilitating forbidden transitions in large enough volumes to be experimentally detectable.

2 Materials and methods

To model spatial variation of the electric field emanating from nano- and sub-nanometer gaps, we first consider a line dipole with a line charge density λ and a gap width of w, fed by an alternating current source of angular frequency ω and surface current density $Ke^{-i\omega t}$ with the charge conservation relationship $K=i\omega\lambda$. In the extreme subwavelength regime of our interest, we can ignore the retarded time, so that the electric field is approximated by the near-field term only [20–26]:

$$\vec{E}(x,z,t)=\frac{\lambda e^{-i\omega t}}{2\pi\varepsilon_0}\left(\frac{\hat{r}_1}{r_1}-\frac{\hat{r}_2}{r_2}\right)= \frac{\lambda e^{-i\omega t}}{2\pi\varepsilon_0}\left[\frac{\left(x-\frac{w}{2},z\right)}{\left(x-\frac{w}{2}\right)^2+z^2}-\frac{\left(x+\frac{w}{2},z\right)}{\left(x+\frac{w}{2}\right)^2+z^2}\right], \quad (1)$$

as plotted in Figure 1A for $w=1$ nm. By replacing λ with $\sigma\,dz$ and integrating over a film thickness of $h=100$ nm, we obtain a realistic field profile of a capacitative nanogap of surface charge density σ, as shown in Figure 1B. For large

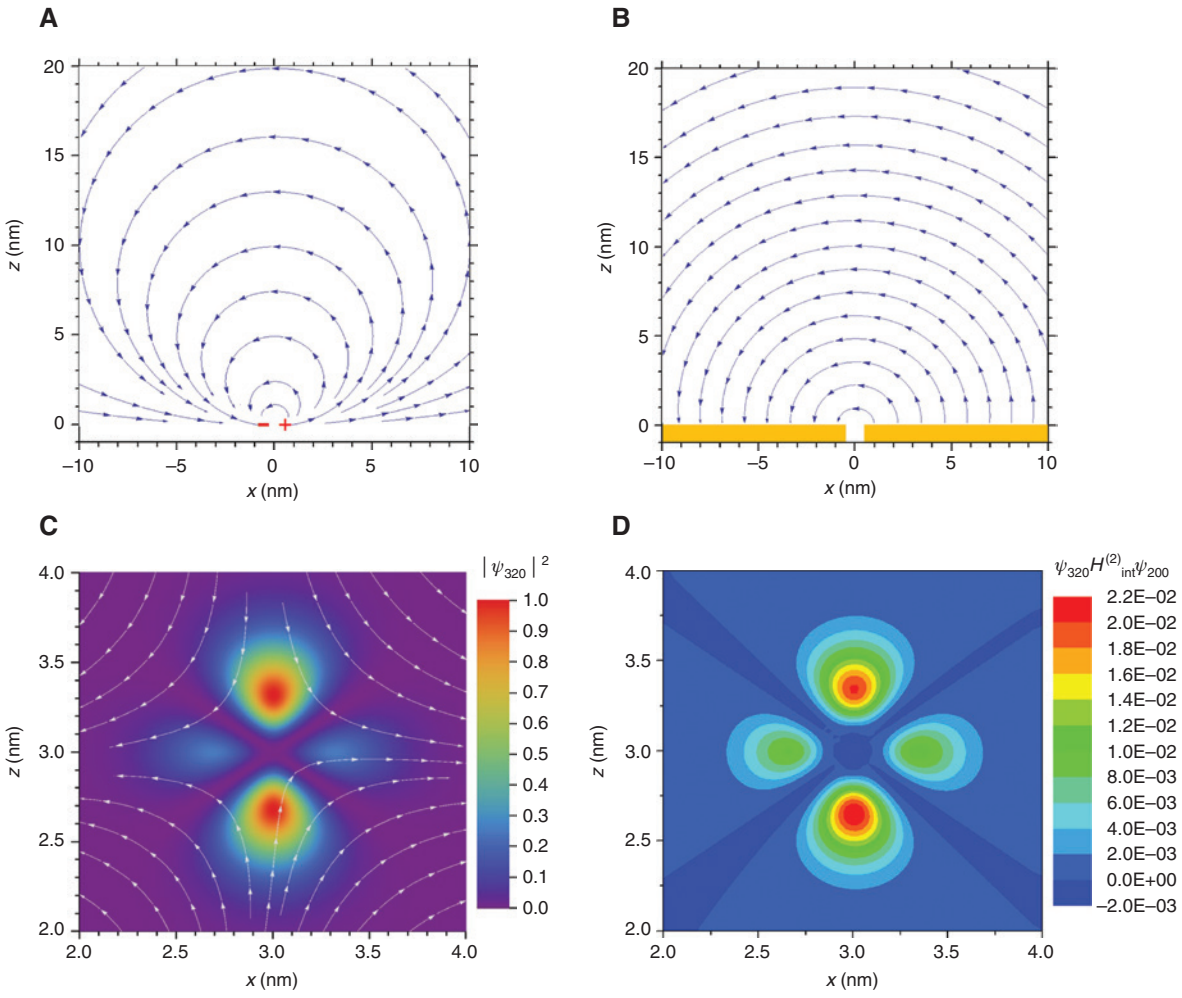

Figure 1: (A) Electric field lines above a line dipole of gap width 1 nm. Line charges are located at $x=\pm0.5$ nm, $z=0$. (B) Electric field profile obtained by an integration of the line dipoles from $z=-100$ to 0 nm, well fitted with an analytical form $\vec{E}(x,z)=\frac{\sigma w}{2\pi\varepsilon_0}\frac{(z,-x)}{x^2+z^2}$ when far away from the gap. (C) Electric field lines $\vec{E}(x,z)-\vec{E}(x_0,z_0)$ around a center position of $(x_0, z_0)=(3\text{ nm}, 3\text{ nm})$ together with $|\psi_{320}(x, 0, z)|^2$. The color scale is in arbitrary units and we use the integrated field profile of Eq. (2). (D) Contour plot of an xz cross section of the overlap integrand $\psi_{320}H^{(2)}_{int}\psi_{200}$ around the center position of (x_0, z_0) (3 nm, 3 nm). The color scale is in arbitrary units.

enough $h << w$, this field is well approximated by a simple form:

$$\vec{E}(x,z,t)=\frac{\sigma w}{2\pi\varepsilon_0}\frac{(z,-x)}{x^2+z^2}e^{-i\omega t} \tag{2}$$

for distances larger than w but smaller than h. Unless otherwise indicated, calculations are performed using the integrated field profile of Eq. (2) using Mathematica and Matlab.

3 Results

We now place a hydrogen atom at a position (x_0, z_0) in a field profile given as Eq. (3), and ask how the transition rates between different states will change relative to the case of a plane wave excitation. Near the source, say, at a position of $(x_0, z_0)=(3\text{ nm}, 3\text{ nm})$, the field lines are curved in the scale of the 3D wavefunctions of a hydrogen atom. It behooves us to examine the behavior of the electric field and the interaction Hamiltonian at the near field. Plotted in Figure 1C at $(x_0, z_0)=(3\text{ nm}, 3\text{ nm})$ are the electric field lines minus their central value, $\vec{E}(x,z)-\vec{E}(x_0,z_0)$, with an xz cross section of the 3D wavefunction $|\psi_{320}|^2$ (n = 3; $l=2$; m = 0) in an area of 2 nm by 2 nm squared. The field lines approximate those of a vector field $(x', -z')$, with $(x, z)\equiv(x_0+x', z_0+z')$, producing an interaction Hamiltonian with a symmetry of $x'^2-z'^2$, as can be seen clearly when we expand around (x_0, z_0):

$$H_{\text{int}}=e\phi(x,z)-e\phi(x_0,z_0)=e\sum_{n=1}^{\infty}\frac{1}{n!}\left(x'\frac{\partial}{\partial x'}+z'\frac{\partial'}{\partial z'}\right)^n \phi(x'+x_0,z'+z_0)\Big|_{x'=z'=0}\approx H_{\text{int}}^{(1)}+H_{\text{int}}^{(2)}+\cdots, \tag{3}$$

where e is the electron charge.

The first term is the dipole approximation Hamiltonian that gives rise to the usual selection rules, whereas the second term contains all the salient features:

$$H_{\text{int}}^{(2)}=e\frac{1}{2}\left(x'\frac{\partial}{\partial x'}+z'\frac{\partial}{\partial z'}\right)^2\phi(x'+x_0,z'+z_0)\Big|_{(x'=0,\,z'=0)} =e\frac{(x'^2-z'^2)}{2}\frac{\partial E_z}{\partial z}\Big|_{(x=x_0,\,z=z_0)}-ex'z'\frac{\partial E_z}{\partial x}\Big|_{(x=x_0,\,z=z_0)} \tag{4}$$

having taken advantage of the divergence relation $\frac{\partial E_x}{\partial x}+\frac{\partial E_z}{\partial z}=0$. To see how this Hamiltonian consisting of two-dimensional quadrutic polynomials can be taken advantage of by the D waves, we resume our interest in the 2S to 3D transition. With the photon energy of $13.6\text{ eV}\left(\frac{1}{4}-\frac{1}{9}\right)=1.89\text{ eV}$ (656 nm) well within the visible range, we can produce the essentially cylindrical field profile near the nanogap using common transition metals. In Figure 1D, the y cross section of the overlap integrand $\psi_{320}H_{\text{int}}^{(2)}\psi_{200}$ is shown in a 2 nm by 2 nm area with the hydrogen nucleus at $(x_0, z_0)=(3\text{ nm}, 3\text{ nm})$. The integrand $\psi_{320}H_{\text{int}}^{(2)}\psi_{200}$ stays mostly *positive*, because the symmetries of $z'^2-x'^2$ from the Hamiltonian and $2z'^2-x'^2$ from ψ_{320} are quite similar. This result suggests that there will be a significant transition matrix element between 2S and 3D states, especially at the vicinity of the gap.

Note that $\psi_{322}\equiv\frac{\psi_{32+2}+\psi_{32-2}}{\sqrt{2}}$ also couples to ψ_{200} through $z'^2-x'^2$, with a matrix element smaller by a factor $\sqrt{3}$, whereas the $-ex'z'\frac{\partial E_z}{\partial x}\Big|_{(x=x_0,z=z_0)}$ part of the Hamiltonian does not participate significantly along the $x=z$ line since $\left|\frac{\partial E_z}{\partial x}\right|\approx 0$ along this line. Clearly, for general directions we also need to consider excitations into ψ_{32+1} and ψ_{32-1} through $x'z'$.

To quantify how strong the forbidden transition matrix elements are between 2S and 3D states, we recall transition dipole moments of allowed excitations. Choosing a local electric field orientation as the z direction, a relevant dipole moment is defined as

$$d_{\text{allowed}}=\frac{\left|\langle\psi_f|H_{\text{int}}|\psi_i\rangle\right|}{E_0}=\frac{\left|\langle\psi_f|eE_0z|\psi_i\rangle\right|}{E_0}=\left|\langle\psi_f|ez|\psi_i\rangle\right|\sim ea_B,$$

where E_0 is the electric field strength at the hydrogen nucleus and a_B is the Bohr radius. Analogously, we define the transition dipole moment of a forbidden 2S to 3D excitation such that

$$d_{200\to320}=\frac{\left|\langle\psi_{320}|H_{\text{int}}|\psi_{200}\rangle\right|}{E_0(x_0,z_0)}.$$

In Figure 2, we quantify forbidden dipole moments of the 2S to 3D transitions. We calculate the total forbidden dipole/transition moment $d_{2S\to3D}=\sqrt{\sum_m d_{200\to32m}^2}$ along the $x=z$ line, as shown in Figure 2A. Calculations using the full H_{int} are represented by blue squares, while those using only $H_{\text{int}}^{(2)}$ are represented by a blue line, displaying near perfect agreement. Finally, taking advantage of $\frac{\left|\frac{\partial E_z}{\partial z}\right|}{|E(x,z)|}\approx\frac{1}{|x|}$ and $\left|\frac{\partial E_z}{\partial x}\right|\approx 0$ along this line, we reach the

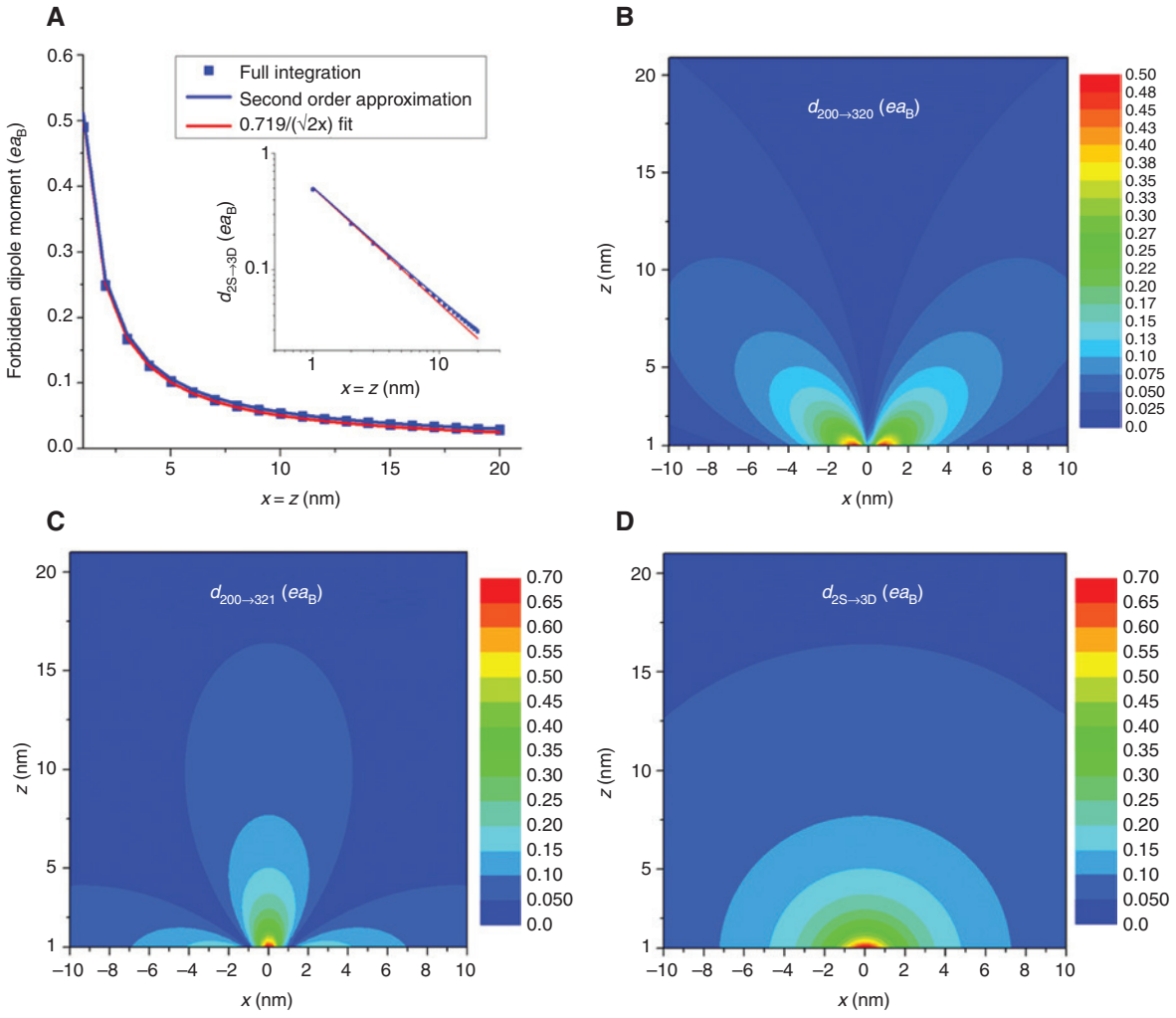

Figure 2: (A) Total forbidden dipole moment along the $x=z$ line, calculated from the second-order Hamiltonian (blue line), the full interaction Hamiltonian (blue squares), and a fit to the analytical expression $0.719/\sqrt{2z}$ (red line). (B) Contour plot of the forbidden transition moment $d_{200\to320}=\frac{|\langle\psi_{320}|H_{int}|\psi_{200}\rangle|}{E_0(x_0,z_0)}$ in units of ea_B where a_B is the Bohr radius, in a 20 nm by 20 nm area starting from $z=1$ nm. (C) Contour plot of the forbidden transition moment $d_{200\to321}=\frac{|\langle\psi_{321}|H_{int}|\psi_{200}\rangle|}{E_0(x_0,z_0)}$. (D) Contour plot of the total forbidden transition moment $d_{2S\to3D}=\sqrt{d^2_{200\to320}+d^2_{200\to322}+d^2_{200\to321}}$. The cylindrical symmetry is largely restored.

simple closed form approximation for the total forbidden dipole moment:

$$d_{2S\to3D}\approx\frac{\sqrt{\left|\langle\psi_{320}\left|\frac{x'^2-z'^2}{2}\right|\psi_{200}\rangle\right|^2+\left|\langle\psi_{322}\left|\frac{x'^2-z'^2}{2}\right|\psi_{200}\rangle\right|^2}\frac{eE_0}{x_0}}{E_0}$$
$$=\frac{2^{16}3^4}{5^8}\frac{ea_B^{\,2}}{\sqrt{2x_0}}\approx13.6ea_B\frac{a_B}{\rho_0}, \quad (5)$$

represented by a red line. In unit of ea_B the red line corresponds to $\frac{0.719}{\sqrt{2x_0}}=\frac{0.719}{\rho_0}$, where x_0 and the distance from the origin ρ_0 are in nanometers. All three results agree rather well.

To see the angular dependences of various forbidden excitations, we plot $\sqrt{d^2_{200\to320}+d^2_{200\to322}}$ in Figure 2B, demonstrating that indeed excitations into ψ_{322} and ψ_{320} are maximum along the $x=z$ line. Transition dipole moments into $\psi_{321}=\frac{\psi_{32+1}+\psi_{32-1}}{\sqrt{2}}$, $d_{200\to321}$, are plotted in Figure 2C, showing an almost orthogonal angle dependence from that of $\sqrt{d^2_{200\to320}+d^2_{200\to322}}$. Adding all the forbidden dipoles, an almost isotropic $d_{2S\to3D}=\sqrt{d^2_{200\to320}+d^2_{200\to321}+d^2_{200\to322}}$

is obtained (Figure 2D), fitted rather well with the simple analytical expression of $\frac{0.719}{\rho_0}$ now applicable to all directions within an error of 0.2–2%, as we move away from the z-axis towards the x-axis.

We now study the width dependence of the forbidden transitions. Since the cylindrical symmetry of the total forbidden dipole moment is only approximate in our geometry, we expect to find deviations as we increase the gap width. Figure 3A depicts the case of $d_{2S\to 3D}$ for $w=3$ nm. Away from the gap, the cylindrical symmetry is recovered, whereas for distances less than 5 nm, angular deviations and weaker moments are evident. For $w=10$ nm in Figure 3B, the deviations are more pronounced, but again, at distances larger than 10 nm, the forbidden dipole moment converges to those of narrower gaps. Figure 3C plots the forbidden dipole moment along the z-axis for several gap widths. For gap widths of 3, 5, and 10 nm, the forbidden dipole moments eventually converge to the $1/z$ line at $z\sim w$. Scanning along the x-direction for a fixed $z=1$ nm, the behavior is very different. At $x=0$, forbidden dipole moments are smaller mainly because along the middle of the gap, field curvatures are less. For $w=3$, 5, and 10 nm, $d_{2S\to 3D}$ peaks at $x\approx\frac{w}{2}$ because sharp edges of the charge distributions are located at $\left(x=\pm\frac{w}{2}, z=0\right)$. Again, at all instances $d_{2S\to 3D}$ recovers the $\frac{0.719}{\rho_0}$ dependence for $x>10$ nm.

We now consider the excited state wavefunction

$$|\psi_{ex}\rangle \propto |\psi_{321}\rangle\langle\psi_{321}|H_{int}|\psi_{200}\rangle + |\psi_{320}\rangle\langle\psi_{320}|H_{int}|\psi_{200}\rangle + |\psi_{322}\rangle\langle\psi_{322}|H_{int}|\psi_{200}\rangle \quad (6)$$

at various locations and conditions. The near-perfect cylindrical symmetry of $d_{2S\to 3D}$ for the 1 nm gap case suggests a strong symmetry for $|\psi_{ex}\rangle$ as well. Figure 4A displays the excited state wavefunction squared using the full interaction Hamiltonian at three different locations.

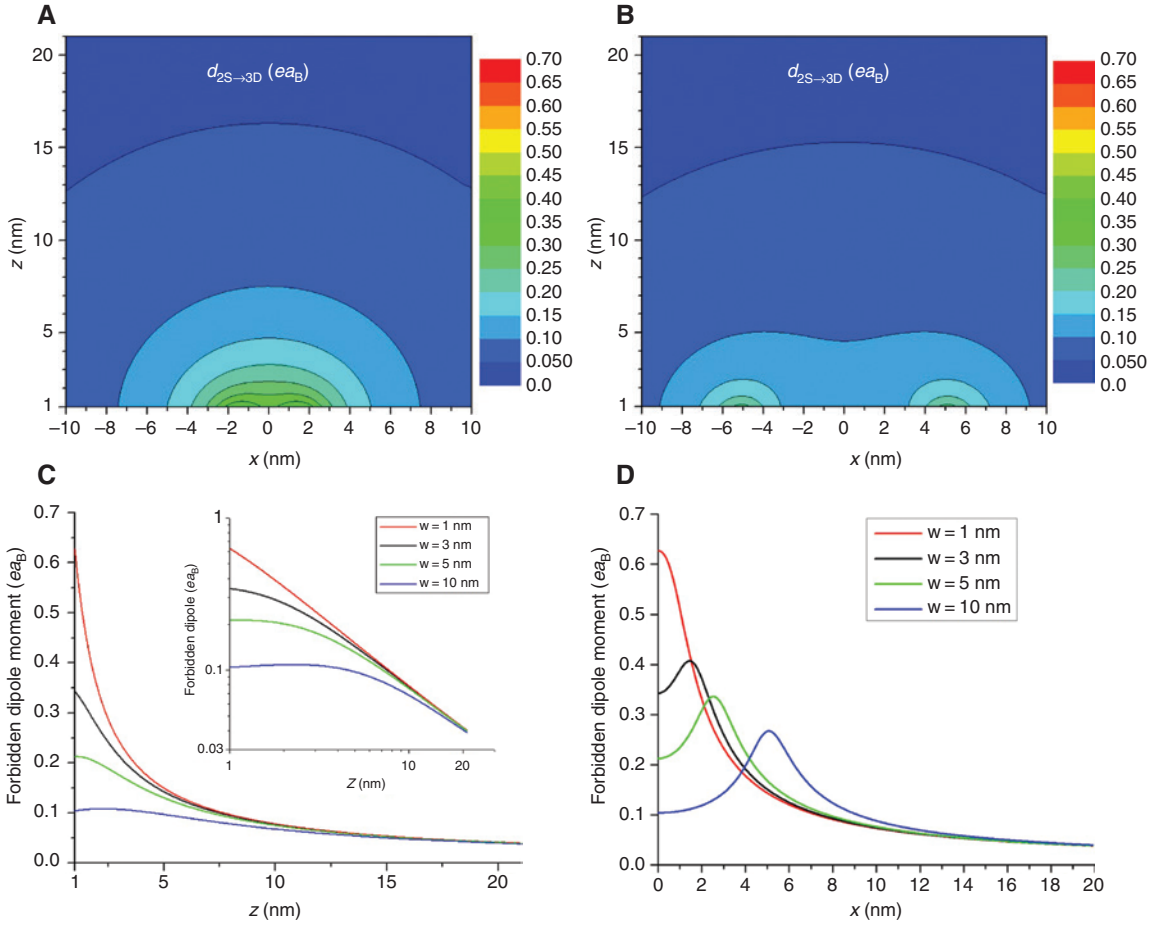

Figure 3: Total forbidden dipole moment $d_{2S\to 3D}$ plotted (A) when $w=3$ nm and (B) when $w=10$ nm. (C) Total forbidden dipole moment along the z-axis when $w=1$, 3, 5, and 10 nm. (Inset: a log-log plot). (D) Total forbidden dipole moment when the observation is along the x-axis keeping $z=1$ nm for $w=1$, 3, 5, and 10 nm.

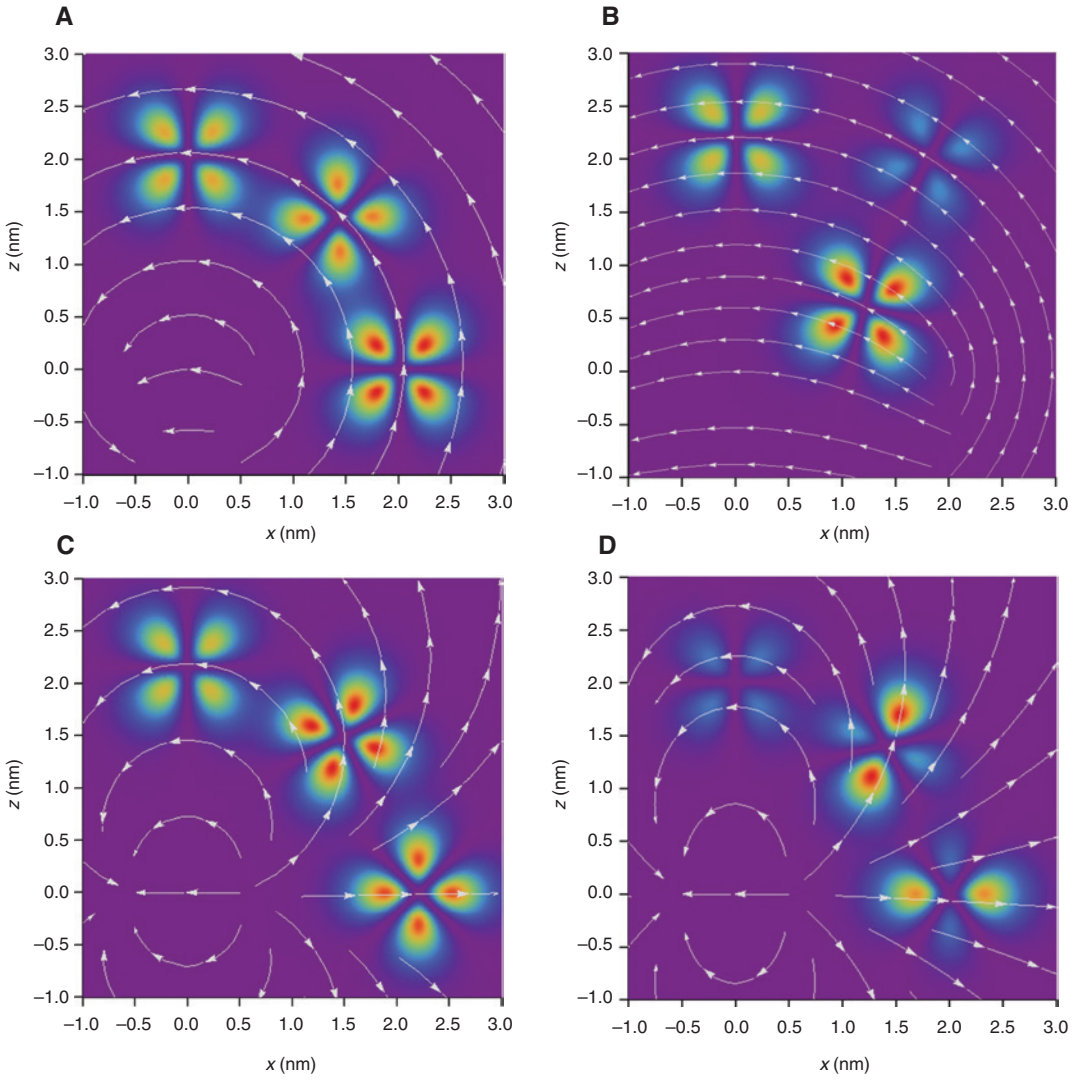

Figure 4: Plot of the *xz* cross section of the excited state wavefunction as defined in Eq. (6), at strategic locations under various conditions. (A) $w = 1$ nm with a cylindrical field profile described in Figure 1B, generated by integrating line dipoles from $z = -100$ to 0 nm, approximated by Eq. (2). (B) Same as (A) except $w = 4$ nm. (C) $w = 1$ nm using the line dipole field of Eq. (1), depicted in Figure 1A. (D) Excited state wavefunctions with a point dipole source. Unlike those excited by the infinite line sources, the wavefunctions are not of a uniform shape.

The excited state wavefunctions faithfully reproduce a pure $|\psi_{321}\rangle$ state within a coordinate system defined by the local field orientation. While physically intuitive, mathematically it is because $\frac{(x^2 - z^2)}{2}\frac{\partial E_z}{\partial z} = xz\frac{\partial E_z}{\partial x}$ when using the field profile of Eq. (2). We found that even with larger gap widths, excited wavefunctions' orientations following the local field orientation remain largely unaffected except for right above the sharp edge (Figure 4B). In stark contrast, as shown in Figure 4C, the single wire case described by Eq. (1) displays wavefunctions not rotating with the local field orientation in a simplistic way. In spite of this complication, the excited wavefunctions remain a pure $|\psi_{321}\rangle$ state at a properly rotated coordinate system, which directly follows from the Hamiltonian of Eq. (4) containing only two quadratic terms: $(x^2 - z^2)$; $2xz$. Replacing our source by a simple point dipole and using Eq. (6) with three-dimensional Hamiltonian produce a whole combination of D wavefunctions evident in Figure 4D. On the equator relative to the dipole orientation, pure $|\psi_{321}\rangle$ still get excited, whereas at most of other directions, all three states contribute.

4 Discussion and conclusion

With the 2S to 3D transition being essentially allowed near the gap, we estimate the spontaneous decay lifetime from

3D to 2S states. An effective dipole moment of one Bohr radius gives rise to a lifetime of 44 ns, six orders of magnitudes faster than the quadrupole transition in the vacuum. The physics of this spontaneous emission modification by nanostructures [27, 28] is clear in our case: in vacuum, the quadrupole transition is weaker than the dipole transition by $\sim\left(\frac{2\pi a_B}{\lambda_0}\right)^2$, where λ_0 is the wavelength of light; on the other hand, near the nanogap with a distance of ρ, we replace this factor by $\sim\left(\frac{2\pi a_B}{\rho}\right)^2$, resulting in fast lifetimes comparable to those of the allowed transitions. Our infinite nanogaps have the advantage over point gaps in that it stretches to millimeter to centimeter length scale in the *y*-axis [11, 12], offering more robustness and million times larger effective areas than point gaps [29]. In attempts to break selection rules by going to shorter wavelength light, for example, X-rays [30], the transitions necessarily involve core orbitals of comparable short length scale, so that the effect is less dramatic than that presented here. Finally, while our technique applies to any S to D transitions, it may not apply to 1S to 3S transitions such as described in [31]. This is because the quadratic potential still gives rise to zero matrix element between two S states because of symmetry.

Our two-dimensional quadratic potentials have, in addition to the obviously larger volume, another advantage over point source dipoles that also give rise to forbidden transitions in surface-enhanced Raman scattering and infrared absorption [23–26] in molecules. The excited wavefunctions are all of one nature, as shown in Figure 4A–C, which can give rise to constructive interference of quadrupole radiations. Finally, while an analytical field profile has been used throughout our paper, a COMSOL calculation assuming a 1 nm gap sandwiched by aluminum layers of 100 nm thickness at 656 nm produces a field profile of a cylindrical symmetry well described by Eq. (2). Finite-difference-time-domain calculations as well as vector field mapping experiments also support this picture [5, 32–34]. We therefore expect similar quantum mechanical results under finite elements electromagnetic simulations.

In conclusion, we have shown that the 2S-3D forbidden transition is allowed for all practical purposes, near the vicinity of a metallic nanogap. The relevant scale of this quadrupole transition becomes not the wavelength of light but the gap width and the distance of the atom from the gap. With million times larger effective volume than point gaps, together with the highly symmetric excited state wavefunctions, we foresee an intimate interaction between atomic spectroscopy and now mature nanogap technology in the near future, especially with free standing gaps. With the advantage of metallic nanogaps of infinite length with an ultimate field enhancement [32] whereby electromagnetic waves from microwaves to ultraviolet have all the same near-field profile [33, 34], up to the plasma frequency of metal, selection rule-free spectroscopy of atoms, molecules, and quantum dots will become of wide use.

Acknowledgments: This work was supported by the National Research Foundation of Korea (NRF) grant funded by the Korea government (MSIP: NRF-2015R1A3A2031768) (MOE: BK21 Plus Program-21A20131111123). DSK acknowledges COMSOL simulations of Taehee Kang and helpful discussions with professors Do-Young Noh, Yongil Shin, Changyoung Kim, and Jae-Hoon Park.

References

[1] Jitrik O, Bunge CF, Carlos F. Transition probabilities for hydrogen-like atoms. J Phys Chem Ref Data 2004;33:1059–70.
[2] Wiese WL, Fuhr JR. Accurate atomic transition probabilities for hydrogen, helium, and lithium. J Phys Chem Ref Data 2009;38:565–719.
[3] Hansch TW, Lee SA, Wallenstein R, Wieman C. Doppler-free two-photon spectroscopy of hydrogen 1S-2S*. Phys Rev Lett 1974;34:307–9.
[4] Lamb WE Jr, Retherford RC. Fine structure of the hydrogen atom by a microwave method. Phys Rev 1947;72:241–3.
[5] Lee KG, Kihm HW, Kihm JE, et al. Vector field microscopic imaging of light. Nat Photon 2007;1:53–6.
[6] Choi SB, Park DJ, Jeong YK, et al. Directional control of surface plasmon polariton waves propagating through an asymmetric Bragg resonator. Appl Phys Lett 2009;94: 063115–7.
[7] Park HR, Park YM, Kim HS, et al. Terahertz nano-resonators: giant field enhancement and ultrabroadband performance. Appl Phys Lett 2010;96:121106–8.
[8] Seo MA, Park HR, Koo SM, et al. Terahertz field enhancement by a metallic nano slit operating beyond the skin-depth limit. Nat Photon 2009;3:152–6.
[9] Koo SM, Kumar MS, Shin JH, Kim DS, Park NK. Extraordinary magnetic field enhancement with metallic nanowire: role of surface impedance in Babinet's principle for ub-skin-depth regime. Phys Rev Lett 2009;103:263901–4.
[10] Jeong JY, Rhie JY, Jeon WJ, Hwang CS, Kim DS. High-throughput fabrication of infinitely long 10 nm slit arrays for terahertz applications. J Infrared Millim Te 2015;36:262–8.
[11] Lee KH, Jeong JY, Bahk YM, et al. Microwave funneling through sub-10 nm nanogaps. ACS Photon 2016;3:537–42.
[12] Olislager L, Kubo W, Tanaka T, et al. Propagation and survival of frequency-binentangled photons in metallic nanostructures. Nanophotonics 2015;4:324–31.

[13] Rui G, Zhan, Q. Tailoring optical complex fields with nanometallic structures. Nanophotonics 2015;4:2–25.
[14] Khurgin JB, Sun G. How small can "nano" be in a "nanolaser"? Nanophotonics 2012;1:3–8.
[15] Shalaby M, Merbold H, Peccianti M, et al. Concurrent field enhancement and high transmission of THz radiation in nanoslit arrays. Appl Phys Lett 2011;99:041110.
[16] Novitsky A, Zalkovskij M, Malureanu R, Lavrinenko A. Microscopic model of the THz field enhancement in a metal nanoslit. Opt Commun 2011;23:5495–500.
[17] Chen X, Park HR, Pelton M, et al. Atomic layer lithography of wafer-scale nanogap arrays for extreme confinement of electromagnetic waves. Nat Commun 2013;4:2361–6.
[18] Kim JY, Kang BJ, Park JH, et al. Terahertz quantum plasmonics of nanoslot antennas in nonlinear regime. Nano Lett 2015;15:6683–8.
[19] Bahk YM, Kang BJ, Kim YS, et al. Electromagnetic saturation of angstrom-sized quantum barriers at terahertz frequencies. Phys Rev Lett 2015;115:125501.
[20] Jackson JD. Classical electrodynamics. New York, Wiley, 1999.
[21] Bao W, Staffaroni M, Boker J, et al. Plasmonic near-field probes: a comparison of the campanile geometry with other sharp tips. Opt Exp 2013;21:8166–76.
[22] Cuche A, Drezet A, Sonnefraud Y, et al. Near-field optical microscopy with a nanodiamond-based single-photon tip. Opt Exp 2009;17:19969–80.
[23] Takase M, Ajiki H, Mizumoti Y, et al. Selection-fuel breakdown in plasmon-induced electronic excitation of an isolated single-walled carbon nanotube. Nat Photon 2013;7:550–4.
[24] Iida T, Aiba Y, Ishihara H. Anomalous optical selection rule of an organic molecule controlled by extremely localized light field. Appl Phys Lett 2011;98:053108.
[25] Moskovits M, DiLella, DP. Surface-enhanced Raman spectroscopy of benzene and benzene-d_6 adsorbed on silver. J Chem Phys 1980;73:6068–75.
[26] Isawa T, Takenaka M, Taketsugu T. Generalized theoretical method for the interaction between arbitrary nonuniform electric field and molecular vibrations: toward near-field infrared spectroscopy and microscopy. J Chem Phys 2016;144:124116.
[27] Pelton M. Modified spontaneous emission in nanophotonic structures. Nat Photon 2015;9:427–35.
[28] Hakhumyan G, Leroy C, Mirzoyan R, Pashayan-Leroy Y, Sarkisyan D. Study of "forbidden" atomic transitions on D2 line using Rb nano-cell placed in external magnetic field. Eur Phys J D 2012;66:119.
[29] Jain PK, Ghosh D, Baer R, Rabani E, Alivisatos AP. Near-field manipulation of spectroscopic selection rules on the nanoscale. Proc Natl Acad Sci USA 2012;109:8016–9.
[30] Demekhin Ph V. On the breakdown of the electric dipole approximation for hard x-ray photoionization cross sections. J Phys B At Mol Opt Phys 2014;47:025602.
[31] Yost DC, Matveev A, Grinin A, et al. Spectroscopy of the hydrogen 1S-3S transition with chirped laser pulses. Phys Rev A 2016;93:042509.
[32] Bahk YM, Han S, Rhie J, et al. Ultimate terahertz field enhancement of single nano slits. Phys Rev B 2017;95:075424.
[33] Ahn JS, Kang T, Singh DK, et al. Optical field enhancement of nanometer-sized gaps at near-infrared frequencies. Opt Exp 2015;23:4897–907.
[34] Kang T, Rhie J, Park J, et al. Resonance tuning of electric field enhancement of nanogaps. Appl Phys Exp 2015;8:092003.